remote sensing

MDPI

Article

Ground Maneuvering Target Focusing via High-Order Phase Correction in High-Squint Synthetic Aperture Radar

Lei Ran *, Zheng Liu and Rong Xie

National Laboratory of Radar Signal Processing, Xidian University, Xi'an 710071, China; lz@xidian.edu.cn (Z.L.); rxie@mail.xidian.edu.cn (R.X.)

* Correspondence: rl@xidian.edu.cn

Abstract: Moving target imaging in high-squint synthetic aperture radar (SAR) shows great potential for reconnaissance and surveillance tasks. For the desired resolution, high-squint SAR has a long-time coherent processing interval (CPI). In this case, the maneuvering motion of the moving target usually causes high-order phase terms in the echoed data, which cannot be neglected for precise focusing. Many ground moving target imaging (GMTIm) algorithms have been proposed in the literature, but some high-order phase terms remain uncompensated in high-squint SAR. For this problem, a high-order phase correction-based GMTIm (HPC-GMTIm) method is proposed in this paper. We assumed that the target of interest has a constant velocity in the subaperture CPI, but maneuvering motion parameters for the whole CPI. Within the short subaperture CPI, the target signal can be simplified as a three-order phase expression, and the instantaneous Doppler frequency (DF) was estimated by some time–frequency analysis tools, including the Hough transform and the fractional Fourier transform. For the whole CPI, the subaperture, the instantaneous DF was combined to form a total least-squares problem, outputting the undetermined phase coefficients. Using the proposed local-to-global processing chain, all high-order phase terms can be estimated and corrected, which outperforms existing methods. The effectiveness of the HPC-GMTIm method is demonstrated by real measured high-squint SAR data.

Keywords: ground moving target imaging (GMTIm); high-order phase correction; high-squint SAR; maneuvering motion; parameter estimation

Citation: Ran, L.; Liu, Z.; Xie, R. Ground Maneuvering Target Focusing via High-Order Phase Correction in High-Squint Synthetic Aperture Radar. *Remote Sens.* **2022**, *14*, 1514. https://doi.org/10.3390/rs14061514

Academic Editors: Jibin Zheng, Xiaolong Chen, Bo Chen and Junjie Wu

Received: 21 January 2022
Accepted: 18 March 2022
Published: 21 March 2022

1. Introduction

For synthetic aperture radar (SAR), the high-squint imaging mode enhances the flexibility and detection ability of the modern radar system, which makes it more preferable than the conventional broadside mode [1–3]. In high-squint mode, focusing the ground moving target can provide detailed target signatures, which benefits the subsequent detection [4] and classification [5].

In stationary SAR images, the ground moving target is defocused and dislocated due to its unknown motions [6–10]. Generally, the range velocity induces an extra Doppler centroid shift, which causes azimuth dislocation and an additional linear range walk [11]. The cross-range velocity impacts the Doppler rate, which results in cross-range defocusing [12]. In addition, the high-squint SAR has a large coherent processing interval (CPI), where the maneuvering motion of the observed target is usually inevitable [13]. The maneuvering motion parameters, such as the acceleration and acceleration rate, cause high-order phase terms. To achieve accurate focusing, these high-order phase terms should be estimated and corrected.

Ground moving target imaging (GMTIm) mainly contains two processing steps: moving target detection and motion parameter estimation. Moving target detection can significantly improve the target signal-to-noise ratio (SNR) and benefits the subsequent motion parameter estimation. For the target located at the high band of the pulse repetition frequency (PRF), it can be separated from the clutter spectrum in the range–Doppler domain [14]. If the target is submerged by the clutter spectrum, the target energy may be

extracted in the image domain [14]. However, if the target is seriously blurred, high SNR data of the moving target can hardly be achieved by windowing the blurred energy in the image domain. To deal with such a problem, this paper utilized multiple low-resolution subaperture images for moving target detection. In different subaperture images, the stationary clutter is nearly unchanged, while the moving target blur gradually varies over a slow time. In this paper, the dominant blur of the moving target was extracted from each subaperture image and transferred back to the raw data domain. By combining the moving target signal from multiple subapertures together, one can obtain the target signal of the whole CPI with a high SNR.

The next step is to estimate and correct the motion parameters of the moving target. The keystone transform (KT) [15–17] and the Hough transform (HT) [14] can be used for the linear range walk correction (LRWC). The KT eliminates the dependence of the range–frequency by interpolation. However, the KT fails to eliminate the LRWC, when the target has a large radial motion due to Doppler ambiguity. The HT can estimate the slope of the target envelop and perform the LRWC in the presence of Doppler ambiguity. If the range curve exists for the moving target of interest, the second-order KT can be utilized for the range curve correction (RCC) [18,19]. After the LRWC and RCC, the target energy is concentrated in one range cell. For the signal in this range cell, the cross-range phase terms are still influenced by the motion parameters, which need to be further estimated. The fractional Fourier transform (FrFT) [8,20–22] is capable of extracting the Doppler rate, and the third-order Doppler parameter can be estimated by the generalized Hough high-order ambiguity function (GHHAF) transform [18] or the polynomial Fourier transform [11].

To our knowledge, the existing GMTIm algorithms are suitable for broadside imaging and only deal with the second- or third-order phase model. They cannot be applied directly to high-squint mode, since more high-order phase terms should be considered. It is worth noting that high-order phase terms are not only caused by the SAR observation, but also induced by the target maneuvering motion in a large CPI.

In this paper, we propose a flexible radar signal processing method to focus the ground moving target in high-squint SAR, which is named the high-order phase correction GMTIm (HPC-GMTIm) algorithm. First, the whole CPI is divided into multiple subapertures. In each subaperture, the target velocity is assumed to be constant. This assumption is acceptable since the subaperture CPI is very short. As a result, the subaperture signal can be reduced to a three-order phase function. From this three-order phase function, the instantaneous Doppler frequency (DF) can be obtained, using the HT and the FrFT to estimate the Doppler centroid and Doppler rate, respectively. The next step is to estimate the signal phase in the whole CPI. The subaperture DF is combined into a linear system of equations, and the whole CPI phase coefficients are determined by solving a total least-squares problem. The proposed GMTIm algorithm can estimate and correct more high-order phase terms in comparison with the existing methods.

2. Moving Target Signal Model in High-Squint SAR

Figure 1 shows the high-squint SAR geometry containing one moving target. The platform carrying the SAR sensor flies along a straight line parallel with the X-axis with a constant velocity v. The squint angle of the beam center line is θ, and the operational range from the aperture center to the scene center o is r_0. Suppose that a target with azimuth distance x_T moves from position P1 to P2 during the CPI. It is hard to determine the target motion information, since no prior knowledge is available. For example, the moving target may have a constant velocity, acceleration, or time-varying motion parameters. In general, the along-track motion is denoted by vector $\mathbf{\Lambda}_x$, and the cross-track one is defined as $\mathbf{\Lambda}_y$. Both $\mathbf{\Lambda}_x$ and $\mathbf{\Lambda}_y$ contain velocity, acceleration, and high-order motion parameters. As a result, the slant range of the moving target at a slow time t_a can be expressed by:

$$r_T(t_a) = \sqrt{\left[r_0 \sin\theta - v(t_a - t_c) + s(\mathbf{\Lambda}_x)\right]^2 + \left[r_0 \cos\theta - s\left(\mathbf{\Lambda}_y\right)\right]^2} \quad (1)$$

where $t_a \in (-T/2, T/2]$, T is the synthetic aperture time, t_c denotes the aperture center time for the moving target, and $s(\mathbf{\Lambda}_x)$ and $s(\mathbf{\Lambda}_y)$ represent the moving distance in the X- and Y-axis, respectively. Extending (1) into a Q-order Taylor series at $(t_a - t_c)$, we obtain the approximated slant range:

$$r_T(t_a) \approx \sum_{q=0}^{Q} a_q (t_a - t_c)^q \approx \sum_{q=0}^{Q} \alpha_q t_a{}^q \tag{2}$$

where a_q is the qth Taylor coefficient. Symbol α_q is a function of a_q and t_c, which means that α_q is azimuth dependent.

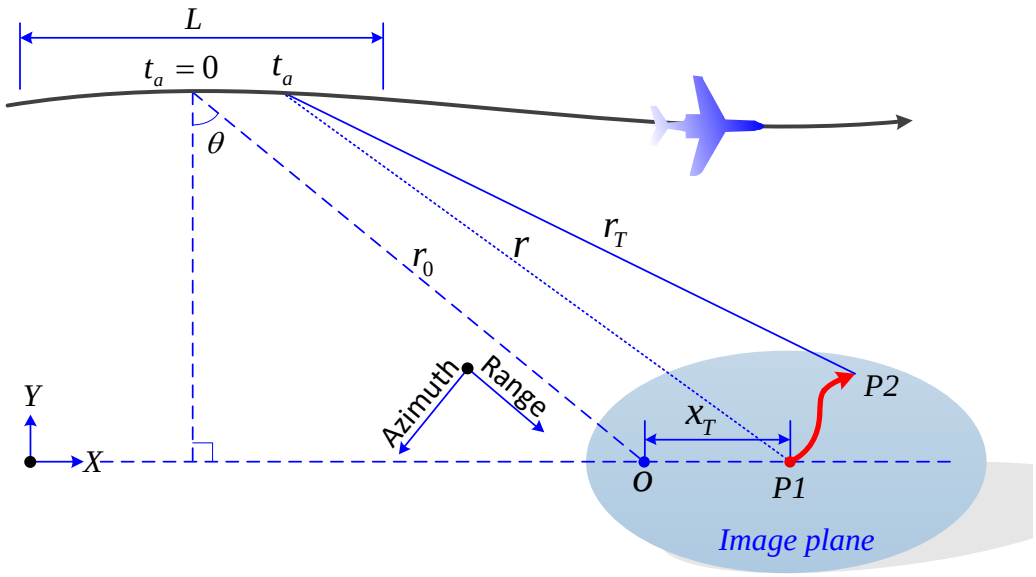

Figure 1. High-squint SAR geometry with a ground maneuvering moving target.

For high-squint SAR imaging, a five-order polynomial has been used in some literature [23]. In the presence of maneuvering motion, more high-order polynomial coefficients should be considered for accurate focusing. The proposed HPC-GMTIm algorithm aims to estimate all Q (α_0 is omitted since it has no effect on focusing) unknown coefficients using a local-to-global processing strategy.

3. The Proposed HPC-GMTIm Algorithm

3.1. Moving Target Detection

In the first type, the moving target Doppler spectrum is located at the high band of the PRF, which means that the moving target energy can be separated from the clutter spectrum in the Doppler domain. Since the moving target spectrum and clutter spectrum do not overlapped, the extracted moving target data have a high SNR. Please see the targets T1 and T3 in the real data experiments in Section 4.

In the second type, the moving target is partially or completely submerged by the clutter spectrum, which implies that the moving target cannot be detected in the Doppler domain. In such a condition, the moving target will be detected in the image domain. However, the moving target may be seriously blurred in the image domain due to the maneuvering motion, for which is difficult to obtain high SNR data. To solve this problem, a moving target detection strategy based on multiple low-resolution subaperture images was developed in this paper. Firstly, all the aperture data are divided into subapertures, and the subaperture images are focused subsequently. The stationary clutter stays nearly unchanged in each subaperture image, while the moving target energy varies with the slow time. Therefore, the moving target can be distinguished visually and extracted from each subaperture image. Finally, the extracted moving target signal in the subaperture image

is transferred back into the raw data domain. By combining the moving target data from multiple subapertures together, one can obtain the target signal in the whole CPI with a high SNR. Examples of the moving target belonging to the second type can be found in Section 4.

3.2. Subaperture Processing

Since the subaperture CPI is quite short, the maneuvering motion of the target can be neglected. Therefore, we assumed that the moving target has a constant velocity within the subaperture CPI, and the slant range at the slow time t_{a_sub} can be simplified as:

$$r_T(t_{a\_sub}) = \sqrt{\left[r_0 \sin\theta - v(t_{a\_sub} - t_c) + v_x(t_{a\_sub} - t_c)\right]^2 + \left[r_0 \cos\theta - v_y(t_{a\_sub} - t_c)\right]^2} \tag{3}$$

where $t_c = x_T/(v - v_x)$, $t_{a\_sub} \in (-T_{sub}/2, T_{sub}/2]$, T_{sub} is the subaperture duration, and v_x and v_y are the along-track and cross-track velocity of the target, respectively. From our experience, the three-order Taylor series of (3) is accurate enough to focus the subaperture signal, which is given by:

$$r_T(t_{a\_sub}) \approx \sum_{k=0}^{3} c_k (t_{a\_sub} - t_c)^k \tag{4}$$

where:

$$\begin{cases} c_0 = r_0 \\ c_1 = -v\sin\theta + v_r \\ c_2 = \frac{(v\cos\theta - v_{cr})^2}{2r_0} \\ c_3 = \frac{(v\cos\theta - v_{cr})^2 (v\sin\theta - v_r)}{2{r_0}^2} \end{cases} \tag{5}$$

and:

$$\begin{cases} v_r = v_x \sin\theta - v_y \cos\theta \\ v_{cr} = v_x \cos\theta + v_y \sin\theta \end{cases} \tag{6}$$

v_r is the range velocity, and v_{cr} is the cross-range one.

Suppose that a pulsed chirp signal $s_t(t_r) = rect(t_r/T_p) \cdot \exp\left[j2\pi\left(f_c t_r + \gamma {t_r}^2/2\right)\right]$ is transmitted. Symbol t_r is the fast time; T_p denotes the pulse width; f_c represents the carrier frequency; γ corresponds to the chirp rate. After removing the carrier frequency, matched-filtering in the range dimension, and transforming the echoed signal into the range–frequency domain, we obtain:

$$\begin{aligned} Ss(f_r, t_{a\_sub}) &= W_r(f_r) w_a(t_{a\_sub} - t_c) \exp\left[-j\frac{4\pi}{c}(f_c + f_r) \sum_{k=0}^{3} c_k (t_{a\_sub} - t_c)^k\right] \\ &= W_r(f_r) w_a(t_{a\_sub} - t_c) \exp\left[-j\frac{4\pi}{c}(f_c + f_r) \sum_{k=0}^{3} \beta_k t_{a\_sub}^k\right] \end{aligned} \tag{7}$$

where $W_r(f_r)$ and $w_a(t_{a\_sub} - t_c)$ are the window function in the range and cross-range dimensions, respectively, c denotes the speed of light, and f_r represents the range frequency. The coefficient β_k is given by:

$$\begin{cases} \beta_0 = r_0 - c_1 t_c + c_2 {t_c}^2 - c_3 {t_c}^3 \\ \beta_1 = c_1 - 2c_2 t_c + 3c_3 {t_c}^2 \\ \beta_2 = c_2 - 3c_3 t_c \\ \beta_3 = c_3 \end{cases} \tag{8}$$

Generally, β_3 makes no contribution to the range cell migration, and the range curve can be corrected by the SAR parameters. Target motion mainly affects the linear range walk

and the azimuth quadratic phase within the subaperture CPI. A simulation experiment was performed to validate these approximations. The simulated parameters are listed in Table 1. There are two targets in the scene. Target 1 is moving with a constant velocity, while target 2 is stationary. Figure 2a shows the linear range walk difference between two targets. It indicates that the target motion causes extra range walk, which cannot be neglected for SAR imaging with a resolution of 1 m × 1 m (range×cross-range). Figure 2b gives the quadratic phase difference between Target 1 and Target 2, which shows that the target motion influences the azimuth focusing. Figure 2c illustrates the third-order azimuth phase difference between the moving target and the stationary one, which implies that the target motion has no effect on the third-order phase. In addition, since the third-order phase is azimuth-independent, it can be deramped by the reference function corresponding to the scene center.

Table 1. Simulated parameters.

Parameter	Value
Operational band	Ku
Squint angle	70°
Platform velocity	100 m/s
Operational range	10 km
Subaperture CPI	1 s
Target 1 coordinate (range, cross-range)	(0, 1000) m
Target 1 velocity (range, cross-range)	(30, 20) m/s
Target 2 coordinate (range, cross-range)	(0, 1000) m
Target 2 velocity (range, cross-range)	(0, 0) m/s

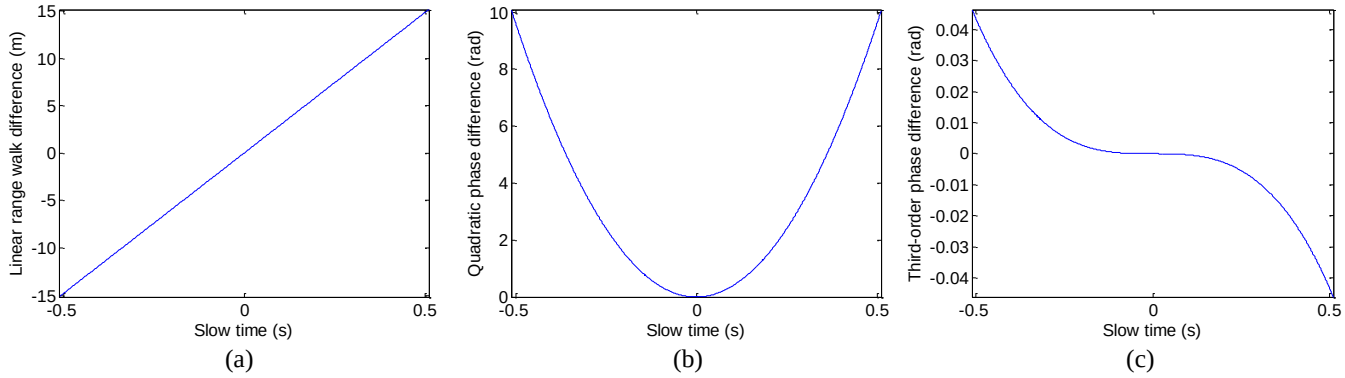

Figure 2. Range: Please add bold for abc in figure, same as others. cell migration and azimuth phase comparison. (**a**) Linear range walk difference. (**b**) Quadratic phase difference. (**c**) Third-order phase difference.

Based on the assumptions above, the range curve of the moving target within the subaperture CPI can be corrected by the SAR parameters. The range curve correction (RCC) function is given by:

$$F_{RCC}(f_r, t_{a\_sub}) = \exp\left[j\frac{2\pi(v\cos\theta)^2}{cr_0}f_r t_{a\_sub}^2\right] \quad (9)$$

It should be mentioned that the moving target range r_0 is unknown, which impacts the precision of the RCC function. Generally, the target moves within a small range area during the subaperture CPI. Therefore, the RCC precision can be guaranteed by using the range center of the data block containing the moving target.

After the RCC, the signal is transferred back to the fast time domain, which is given by:

$$ss(t_r, t_{a\_sub}) = sinc\left\{\gamma T_p\left[t_r - \frac{2\left(\beta_0 + \beta_1 t_{a\_sub}\right)}{c}\right]\right\} \cdot \exp\left(-j\frac{4\pi}{\lambda}\sum_{k=0}^{3}\beta_k t_{a\_sub}^k\right) \quad (10)$$

where λ is the wavelength. Obviously, $\beta_1 t_{a\_sub}$ introduces extra linear range walk in (10). We used the HT to estimate the target envelop slope rate. Then, the linear range walk correction (LRWC) function can be obtained as follows:

$$F_{LRWC}(f_r, t_{a\_sub}) = \exp\left[j\frac{4\pi}{c}(f_c + f_r)\hat{\beta}_1 t_{a\_sub}\right] \quad (11)$$

where $\hat{\beta}_1$ is the target envelop slope rate estimated by the HT.

After the LRWC, the target signal is given by:

$$ss(t_r, t_{a\_sub}) = sinc\left[\gamma T_p\left(t_r - \frac{2\beta_0}{c}\right)\right] \cdot \exp\left[-j\frac{4\pi}{\lambda}\left(\beta_0 + \beta_2 t_{a\_sub}^2 + \beta_3 t_{a\_sub}^3\right)\right] \quad (12)$$

Now, the target energy is concentrated into one range cell. It should be noted that the moving target is located at range β_0 instead of the real one r_0 after the LRWC, which usually causes an azimuth-variant phase in high-squint SAR [23]. From Figure 2, we know that the target motion has no effect on the third-order azimuth phase. Therefore, the third-order phase can be deramped by the reference function corresponding to the scene center, which is given by:

$$F_{3rd\_dmp}(t_{a\_sub}) = \exp\left(j\frac{2\pi v^3 \cos^2\theta \sin\theta}{\lambda {\beta_0}^2} t_{a\_sub}^3\right) \quad (13)$$

Since the real slant range r_0 is unknown, the equivalent one β_0 after the LRWC is used in (13). In (8), $\beta_0 = r_0 - c_1 t_c + c_2 {t_c}^2 - c_3 {t_c}^3$. In airborne SAR, the operational range $r_0 \gg -c_1 t_c + c_2 {t_c}^2 - c_3 {t_c}^3$ within the subaperture CPI. This indicates that the difference between r_0 and β_0 is very small; therefore, the deramping precision can be guaranteed by (13). After the third-order phase correction, the target signal can be expressed by:

$$ss(t_r, t_{a\_sub}) = sinc\left[\gamma T_p\left(t_r - \frac{2\beta_0}{c}\right)\right] \exp\left[-j\frac{4\pi}{\lambda}\left(\beta_0 + \beta_2 t_{a\_sub}^2\right)\right] \quad (14)$$

Next, the FrFT is utilized to estimate the Doppler rate. Then, we can obtain the second-order deramping function as follows:

$$F_{2nd\_dmp}(t_{a\_sub}) = \exp\left(j\frac{4\pi}{\lambda}\hat{\beta}_2 t_{a\_sub}^2\right) \quad (15)$$

where $\hat{\beta}_2$ comes from the estimation result of the FrFT. Multiplying (14) and (15), and performing the azimuth Fourier transform (FT), the target can be focused in the Doppler domain as follows:

$$sS(t_r, f_{a\_sub}) = sinc\left[\gamma T_p\left(t_r - \frac{2\beta_0}{c}\right)\right] sinc\left(\frac{f_{a\_sub}}{B_{a\_sub}}\right) \cdot \exp\left(-j\frac{4\pi}{\lambda}\beta_0\right) \quad (16)$$

where B_{a_sub} is the Doppler bandwidth in the subaperture CPI.

3.3. Whole Aperture Processing

For symbol clarity, we use non-bold symbols to represent scalars and bold symbols to indicate vectors or matrices. The dimensionality of the vectors and matrices is marked by their subscript.

Based on the phase parameters estimated in the last subsection, the instantaneous DF of the moving target in the subaperture CPI can be obtained as follows:

$$DF(m; t_{a\_sub}) = \frac{2}{\lambda}\left[\hat{\beta}_1(m) + 2\hat{\beta}_2(m)t_{a\_sub} + 3\tilde{\beta}_3(m)t_{a\_sub}^2\right] \tag{17}$$

where $\hat{\beta}_1$ is the target envelop slope rate estimated by the HT, $\hat{\beta}_2$ is the Doppler rate obtained by the FrFT, $\tilde{\beta}_3 = \frac{v^3\cos^2\theta\sin\theta}{2{\beta_0}^2}$, and m is the subaperture index, $m = 1, 2, \ldots, M$. In discrete form, the vector containing DF elements of pulses in the subaperture is given by:

$$\boldsymbol{DF}(m) = [DF(m, t_1) \quad DF(m, t_2) \cdots DF(m, t_{N/M})]_{1\times N/M} \tag{18}$$

where N represents the number of pulses in the whole aperture.

Next, the estimated DF components from all the subapertures can be vectorized as:

$$\boldsymbol{\Psi} = [\boldsymbol{DF}(1) \quad \boldsymbol{DF}(2) \quad \cdots \quad \boldsymbol{DF}(M)]_{1\times N}^T \tag{19}$$

where $[\,\cdot\,]^T$ denotes the vector/matrix transpose.

The theoretical DF of the moving target can be calculated by the first-order derivation of Equation (2), which is given by:

$$\boldsymbol{\Omega} = \frac{2}{\lambda}\cdot\frac{\partial r_T(t_a)}{\partial t_a} = \frac{2}{\lambda}\cdot[\delta(n,q)]_{N\times Q} \tag{20}$$

$$\delta(n,q) = q\cdot[t_a(n)]^{q-1} \tag{21}$$

where $n = 1, 2, \ldots, N$, $q = 1, 2, \ldots, Q$. The undetermined coefficients can be vectorized as:

$$\boldsymbol{\alpha} = [\alpha_1 \quad \alpha_2 \quad \cdots \quad \alpha_Q]_{1\times Q}^T \tag{22}$$

Thus, we can obtain the following least-squares problem:

$$\boldsymbol{\Psi} = \boldsymbol{\Omega\alpha} \tag{23}$$

In practical applications, the pre-determined polynomial order Q may be different from the real one, which induces error in the matrix $\boldsymbol{\Omega}$. At the same time, due to the existence of noise and clutter, the DF elements from subaperture processing, i.e., the observation vector $\boldsymbol{\Psi}$, may also contain estimation errors. In such a situation, the total least-squares (TLS) [24–26] kernel helps to improve the estimation precision of Equation (23).

To apply the TLS kernel, singular-value decomposition (SVD) is first performed as follows:

$$[\boldsymbol{\Omega} \quad \boldsymbol{\Psi}] = \boldsymbol{USV}^T \tag{24}$$

where $\boldsymbol{S} \in \Re^{N\times(Q+1)}$ contains the singular values, and $\boldsymbol{U} \in \Re^{N\times N}$ and $\boldsymbol{V} \in \Re^{(Q+1)\times(Q+1)}$ denote the left and right singular matrices, respectively.

Let $\boldsymbol{U}_r = [\boldsymbol{u}_r \quad \boldsymbol{o}]_{N\times N}$, where $\boldsymbol{u}_r$ denotes the left r columns of $\boldsymbol{U}$ and $r \le N$. Substituting $\boldsymbol{U}_r$ with $\boldsymbol{U}$, the approximated linear system can be set up as follows:

$$\boldsymbol{\Psi}_r = \boldsymbol{\Omega}_r\boldsymbol{\alpha} \tag{25}$$

where $\boldsymbol{\Psi}_r = \boldsymbol{U}_r \boldsymbol{S} \boldsymbol{V}_{\boldsymbol{\Psi}}^T$, $\boldsymbol{\Omega}_r = \boldsymbol{U}_r \boldsymbol{S} \boldsymbol{V}_{\boldsymbol{\Omega}}^T$, $\boldsymbol{V} = \begin{bmatrix} \boldsymbol{V}_{\boldsymbol{\Omega}} \\ \boldsymbol{V}_{\boldsymbol{\Psi}} \end{bmatrix}$. Then, the TLS solver can be computed by:

$$\begin{aligned} \hat{\boldsymbol{\alpha}}_{TLS} &= \left({\boldsymbol{\Omega}_r}^T \boldsymbol{\Omega}_r \right)^{-1} {\boldsymbol{\Omega}_r}^T \boldsymbol{\Psi}_r \\ &= \left(\boldsymbol{V}_{\boldsymbol{\Omega}} \boldsymbol{S}^T {\boldsymbol{U}_r}^T \boldsymbol{U}_r \boldsymbol{S} \boldsymbol{V}_{\boldsymbol{\Omega}}^T \right)^{-1} \boldsymbol{V}_{\boldsymbol{\Omega}} \boldsymbol{S}^T {\boldsymbol{U}_r}^T \boldsymbol{U}_r \boldsymbol{S} \boldsymbol{V}_{\boldsymbol{\Psi}}^T \\ &= \left(\boldsymbol{V}_{\boldsymbol{\Omega}} \boldsymbol{S}^T \boldsymbol{U}^T \boldsymbol{U}_r {\boldsymbol{U}_r}^T \boldsymbol{U} \boldsymbol{S} \boldsymbol{V}_{\boldsymbol{\Omega}}^T \right)^{-1} \boldsymbol{V}_{\boldsymbol{\Omega}} \boldsymbol{S}^T \boldsymbol{U}^T \boldsymbol{U}_r {\boldsymbol{U}_r}^T \boldsymbol{U} \boldsymbol{S} \boldsymbol{V}_{\boldsymbol{\Psi}}^T \\ &= \left(\boldsymbol{\Omega}^T \boldsymbol{U}_r {\boldsymbol{U}_r}^T \boldsymbol{\Omega} \right)^{-1} \boldsymbol{\Omega}^T \boldsymbol{U}_r {\boldsymbol{U}_r}^T \boldsymbol{\Psi} \end{aligned} \tag{26}$$

Obviously, $\boldsymbol{U}_r$ is an r-rank approximated matrix of $\boldsymbol{U}$. According to the SVD result, $\boldsymbol{S}$ contains all singular values, and the effective rank r can be determined by the following expression:

$$\zeta(r) = \frac{\|\boldsymbol{S}_r\|_F}{\|\boldsymbol{S}\|_F} = \left(\frac{\sum_{i=1}^{r} {\delta_i}^2}{\sum_{i=1}^{N} {\delta_i}^2} \right)^{1/2} \tag{27}$$

where $\| \cdot \|_F$ is the Frobenius norm and δ_i is the nonzero singular value. To determine the effective rank, one can set a threshold approximated to 1 ($\zeta_T(r) = 0.998$ for example), and r is the smallest integer that satisfies $\zeta(r) \geq \zeta_T(r)$. The TLS solver helps to reduce the effect of errors in $\boldsymbol{\Omega}$ and $\boldsymbol{\Psi}$ on the phase coefficients, thus improving the estimation precision.

Based on the TLS result $\hat{\boldsymbol{\alpha}}_{TLS}$, the range cell migration correction (RCMC) and phase correction for all the aperture data can be performed. The corresponding correction function is given by:

$$Ss(f_r, t_a) = \exp\left[-j \frac{4\pi}{c} (f_c + f_r) \sum_{q=1}^{Q} \hat{\alpha}_q {t_a}^q \right] \tag{28}$$

where $\hat{\alpha}_q \in \hat{\boldsymbol{\alpha}}_{TLS}$. After the range inverse FT and cross-range FT, the moving target can be focused as follows:

$$sS(t_r, f_a) = sinc\left[\gamma T_p \left(t_r - \frac{2\alpha_0}{c} \right) \right] sinc\left(\frac{f_a}{B_a} \right) \exp\left(-j \frac{4\pi}{\lambda} \alpha_0 \right) \tag{29}$$

where B_a is the Doppler bandwidth of the moving target in the whole CPI.

Since the number of DF elements N is much larger than the order of polynomial Q, the proposed HPC-GMTIm algorithm is suitable for a high-order signal model. In practical applications, the proposed method may be performed in an iterative way to improve the focusing precision. In earlier iterations, a short subaperture CPI is recommended for high-order phase estimation, while a large subaperture CPI is suitable for the low-order signal model in later iterations. For clarity, the flowchart of the HPC-GMTIm algorithm is illustrated in Figure 3.

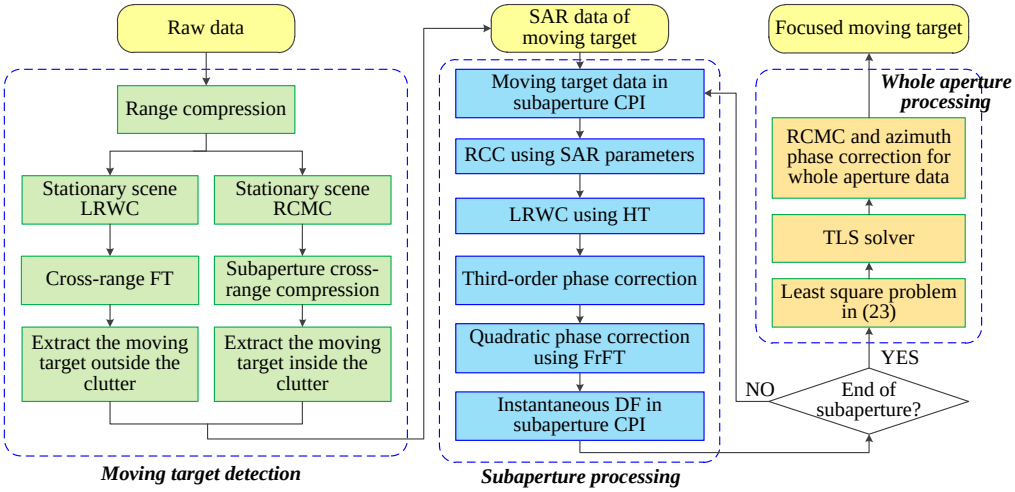

Figure 3. Flowchart of the proposed HPC-GMTIm algorithm.

3.4. Simulation Experiment

A simulation was performed to illustrate the processing details of the HPC-GMTIm algorithm. The simulated parameters are listed in Table 2. All the aperture data were divided into 8 subapertures, and the polynomial order was set as $Q = 7$. There was one moving target in the observed scene, which had maneuvering motion, including a constant velocity, acceleration, and acceleration rate.

Table 2. Simulated parameters.

Parameter	Value
Operational band	17 GHz
Squint angle	70°
Bandwidth	200 MHz
Sample rate	250 MHz
Platform velocity	100 m/s
Operational range	10 km
PRF	1 kHz
Whole CPI	4 s
Subaperture CPI	0.5 s
Resolution (range × cross-range)	1 m × 1 m
Target coordinate (range, cross-range)	(0, 1000) m
Target velocity (range, cross-range)	(30, −20) m/s
Target acceleration (range, cross-range)	(2, 2) m/s^2
Target acceleration rate (range, cross-range)	(0.5, 0.2) m/s^3

For subaperture processing, Figure 4 shows the corresponding subaperture images, which are well focused. After the RCMC and azimuth phase correction for all the aperture data, the moving target can be focused, as shown in Figure 5a. We used the GHHAF method proposed in [18] for the performance comparison. The GHHAF method can only compensate the third-order phase error caused by target motion, which is insufficient for high-squint SAR-GMTIm. As shown in Figure 5, the proposed HPC-GMTIm algorithm achieved better focusing performance than GHHAF. To evaluate the focusing quality, the related peak sidelobe ratio (PSLR), integrated sidelobe ratio (ISLR), and impulse response width (IRW) are listed in Table 3. Obviously, the proposed HPC-GMTIm outperformed the GHHAF method from the aspect of both cross-range profiles and focusing quality values.

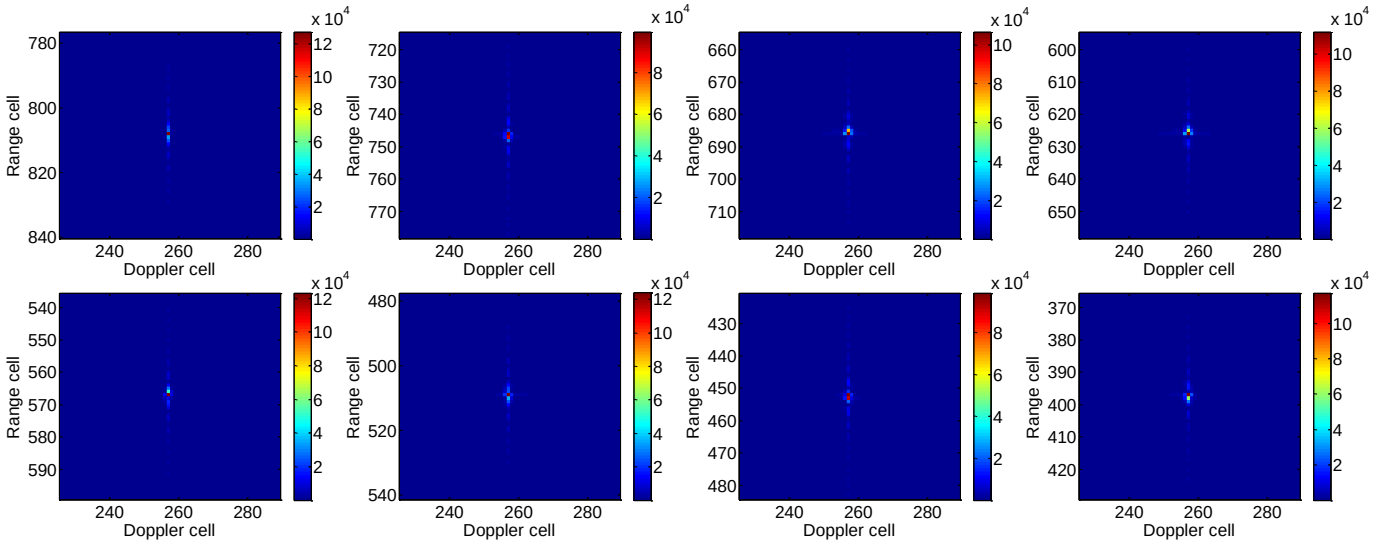

Figure 4. Subaperture processing results. The whole aperture is divided into 8 subapertures, and all 8 subaperture images are well focused by the proposed HPC-GMTIm algorithm.

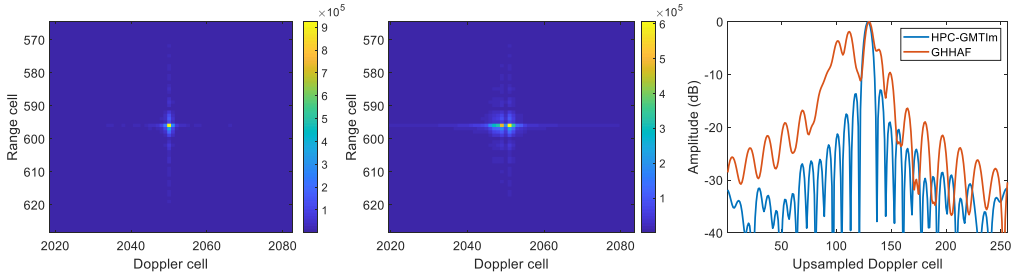

Figure 5. Whole aperture image. (**a**) HPC-GMTIm algorithm. (**b**) GHHAF method. (**c**) Cross-range profile comparison.

Table 3. Focusing quality evaluation.

Methods	PSLR(dB)	ISLR(dB)	IRW(m)
HPC-GMTIm	−12.96	−10.03	0.66
GHHAF	−1.93	−1.89	2.11

3.5. Practical Considerations

(1) **Platform motion errors**: For high-squint SAR mounted on an unmanned aerial vehicle (UAV) [24,27–29] or missile [30], platform motion errors are usually inevitable. If the platform is equipped with a high-precision inertial measurement unit (IMU), motion compensation (MOCO) can be performed using the IMU data. Otherwise, an autofocus technique is needed [3,31,32]. For autofocusing, the stationary scene should be selected to estimate the motion error. Then, MOCO is performed, and the moving target can be processed by the proposed HPC-GMTIm method;

(2) **High resolution imaging**: The higher resolution one desires, the larger the CPI it takes. This means that the target motion becomes more complicated for high-resolution applications. Besides the high-order phase, high-order range cell migration may be induced in the recorded data. In such a condition, the proposed HPC-GMTIm algorithm was still effective, and for that, the assumption of subaperture constant velocity still can be guaranteed by decreasing the subaperture length, while the polynomial order can be set flexibly for high-order range cell migration and phase correction. In addition, more motion vectors, such as rotation and rotation rate [33,34],

become non-negligible for high-resolution imaging, which will be considered in our future work;

(3) **Motion parameters estimation**: In HPC-GMTIm processing, all Q polynomial coefficients are determined, but the target parameters (i.e., velocity, acceleration, acceleration rate, and position) cannot be obtained. This is because the target motion parameters are coupled together, and they cannot be estimated accurately from the undetermined system of equations. Since the motion parameter estimation is a technical obstacle for high-squint SAR GMTIm at present, this paper paid more attention to target focusing.

4. Real Data Experiments

Real datasets collected by an experimental airborne SAR system were used to validate the performance of the HPC-GMTIm algorithm. The system- and data-related parameters are listed in Table 4. There were 4 moving targets to be focused, where targets T1 and T2 were extracted from Dataset 1 and T3 and T4 came from Dataset 2. The imaging result of each target will be shown in the following.

Table 4. Real data parameters.

Parameter	Dataset 1/Dataset 2
Operational band	Ku
Squint angle	50°/70°
Operational range	7.3 km
Synthetic aperture length	175 m
Whole CPI	4 s
Subaperture CPI	0.5 s
Resolution (range×cross-range)	1 m × 1 m/2 m × 2 m

4.1. T1

Target T1 is located at the high band of the PRF, as shown in Figure 6a, which denotes the range–Doppler domain after the LRWC for the stationary scene. Then, the target detection is performed in the range–Doppler domain by windowing the dominant blur of the moving target, as shown in Figure 6b. The corresponding image of the stationary scene is given in Figure 7, where the blur of the moving target cannot be found.

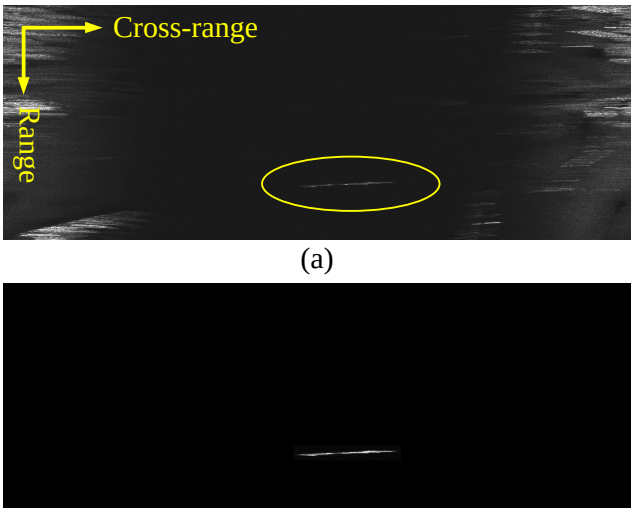

(a)

(b)

Figure 6. Moving target detection for T1. (**a**) Range–Doppler domain. (**b**) Moving target detection result.

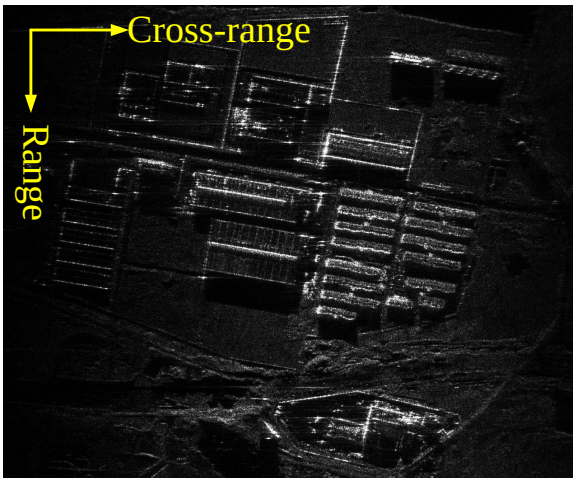

Figure 7. The stationary scene image after eliminating the energy of T1.

After the LRWC for the stationary scene, the envelope of T1 is plotted in Figure 8a. It can be seen that the moving target had serious range cell migration, which indicated that T1 had a large radial velocity. Using the proposed HPC-GMTIm algorithm, the envelope of T1 was confined into one range cell after the RCMC, as illustrated in Figure 8b. T1 can be focused after azimuth high-order phase correction, which is shown in Figure 9a. In the GHHAF method, by contrast, the moving target was still defocused, as given in Figure 9b. The reason for the failure of the GHHAF method was that the high-order phase terms were not estimated and corrected.

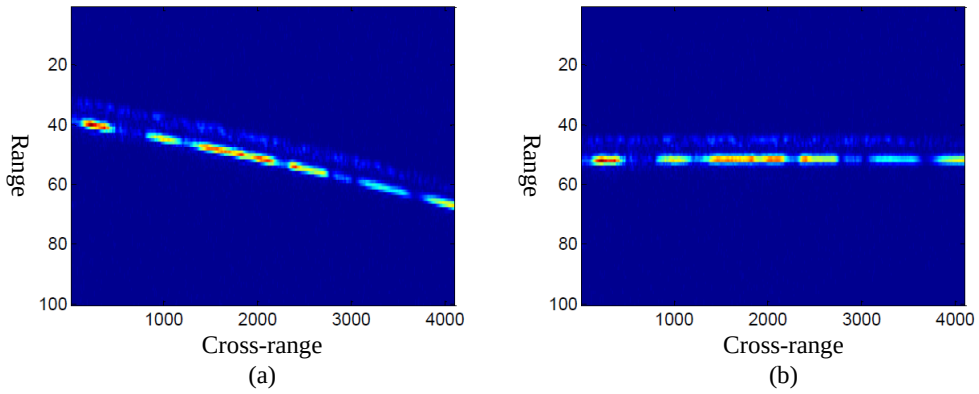

Figure 8. The envelope of T1. (**a**) Before correction. (**b**) After correction.

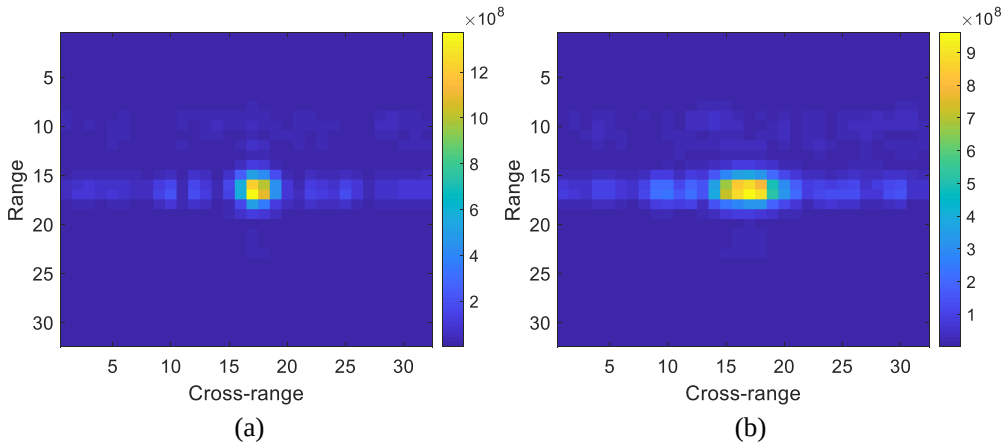

Figure 9. The imaging result of T1. (**a**) HPC-GMTIm (entropy = 2.97). (**b**) GHHAF method (entropy = 3.36).

4.2. T2

The moving target T2 was submerged by the clutter, as shown in Figure 10. Target detection in the image domain by windowing the dominant blur was confronted with serious clutter disturbance, which decreased the moving target SNR. T2 belongs to the second type of target, as discussed in Section 3, and it was detected based on multiple subaperture low-resolution images, which are shown in Figure 11. In each subaperture image, the energy of T2 was reserved, while the clutter area was reduced vastly, thus improving the target SNR after detection.

By transferring the detected data in Figure 11b back to the range-compressed and cross-range slow time domain, the envelope of T2 is plotted in Figure 12a, which contains large range cell migration. After processing by the HPC-GMTIm algorithm, the envelope was corrected into one range cell, as shown in Figure 12b. Figure 13 presents the imaging results of the HPC-GMTIm and GHHAF methods. It is shown that the HPC-GMTIm algorithm outperformed the GHHAF from the viewpoint of focusing, which validates the necessity of high-order phase correction.

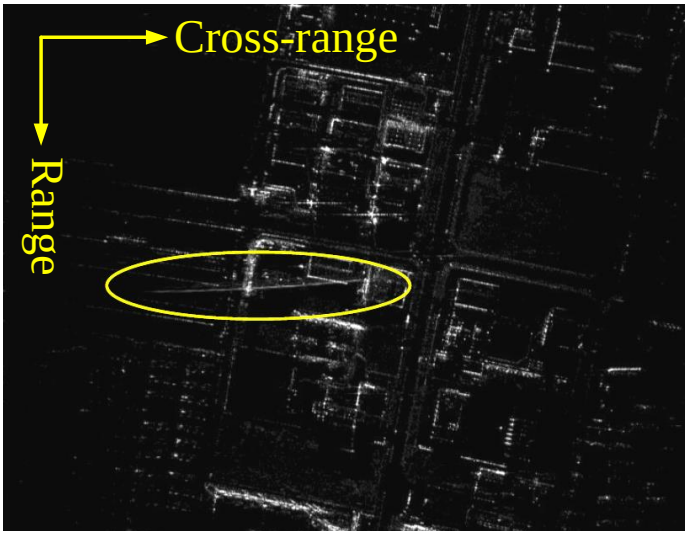

Figure 10. The stationary scene image containing moving target T2.

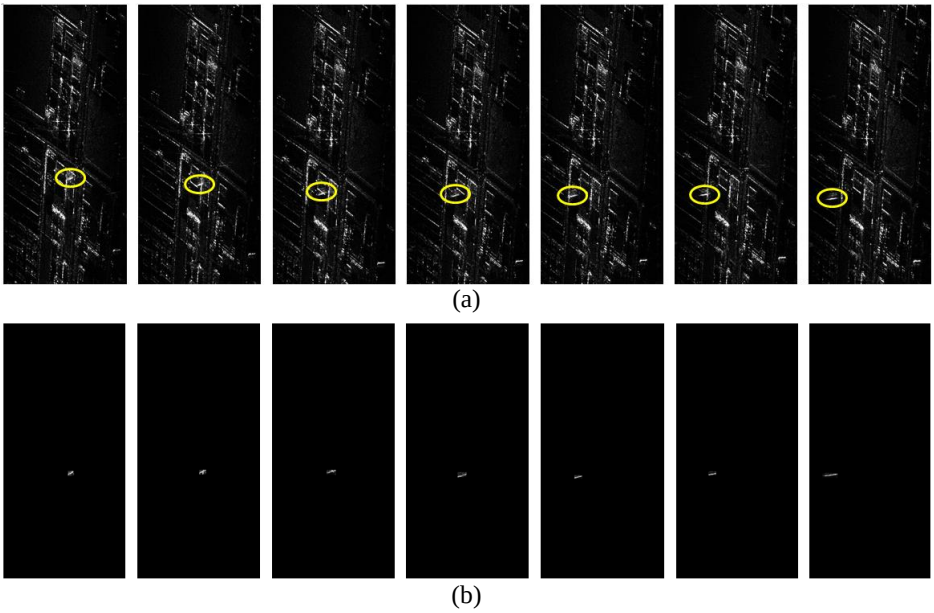

Figure 11. Moving target detection for T2. (**a**) Subaperture images before detection. (**b**) Subaperture images after detection.

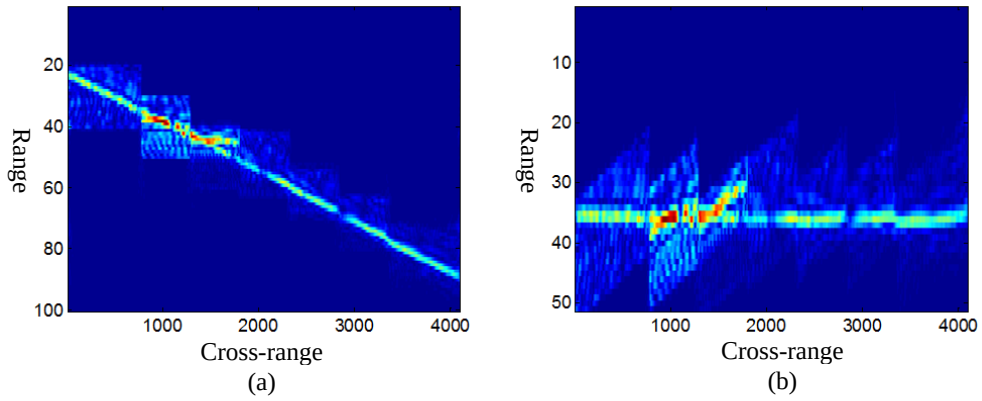

Figure 12. The envelope of T2. (**a**) Before correction. (**b**) After correction.

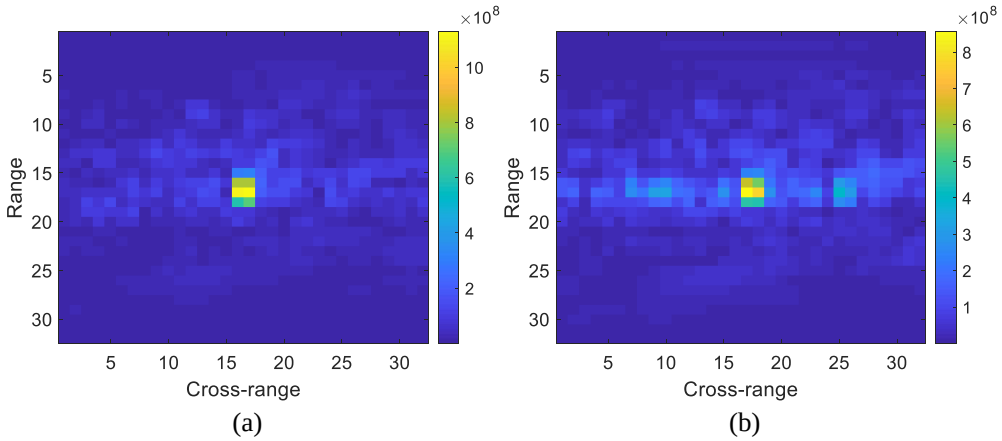

Figure 13. The imaging result of T2. (**a**) HPC-GMTIm (entropy = 3.62). (**b**) GHHAF method (entropy = 4.17).

4.3. T3

Applying the LRWC for the stationary scene and transferring the echo to the Doppler domain, the range–Doppler data are illustrated in Figure 14a. There is one moving target, named T3, outside the clutter spectrum in Figure 14a. The energy of T3 was extracted using a rectangle window around the dominant blur, which is shown in Figure 14b. The related stationary scene is plotted in Figure 15. There is a highway cross in Figure 15, which indicates that moving targets can be observed easily. Figure 16 presents the envelope of T3, where Figure 16a is the envelope after the LRWC using the SAR parameters, and Figure 16b is the one corrected by the HPC-GMTIm algorithm. After azimuth phase compensation, T3 was well focused by the HPC-GMTIm algorithm, while the imaging result of the GHHAF method involved obvious blurring, as shown in Figure 17.

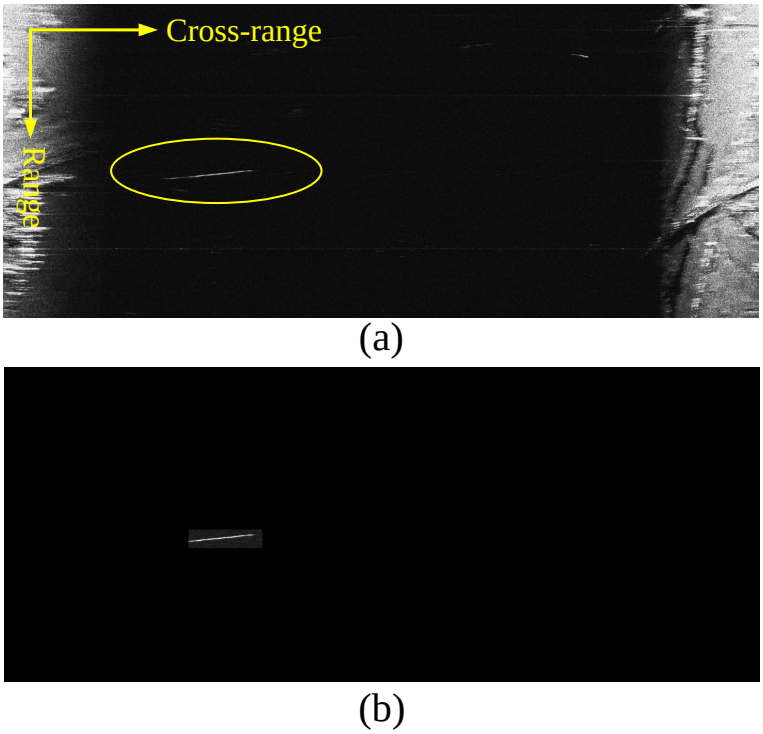

Figure 14. Moving target detection for T3. (**a**) Range–Doppler domain. (**b**) Moving target detection result.

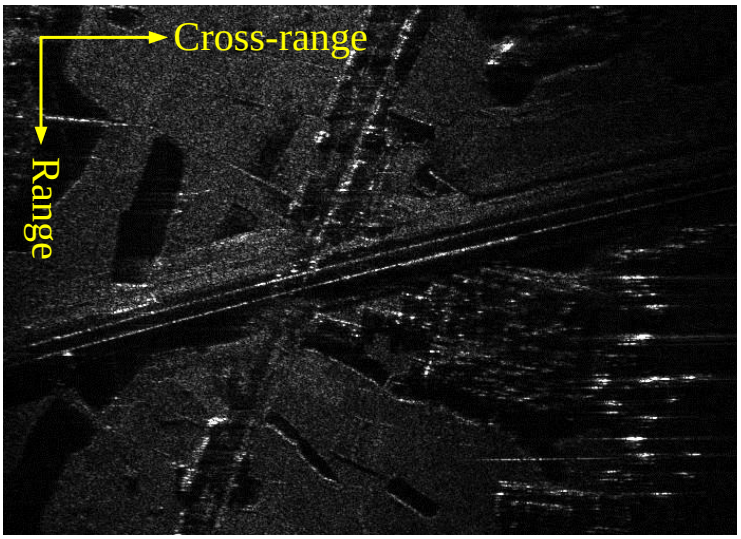

Figure 15. The stationary scene image corresponding to T3.

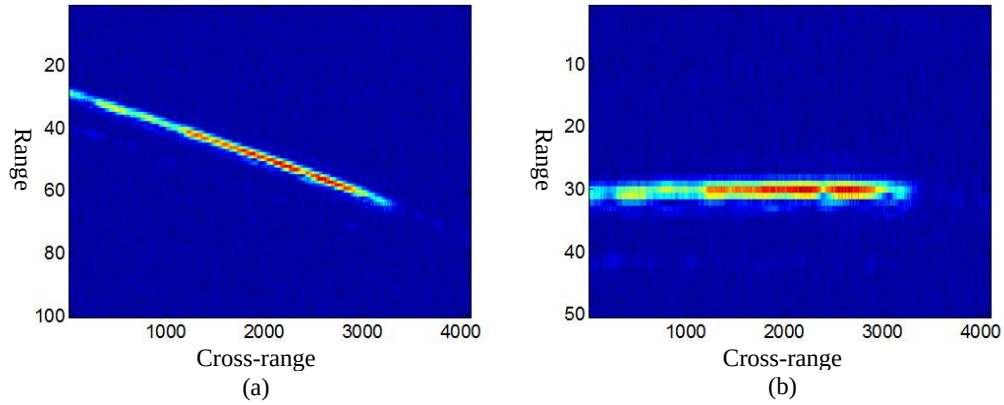

Figure 16. The envelope of T3. (**a**) Before correction. (**b**) After correction.

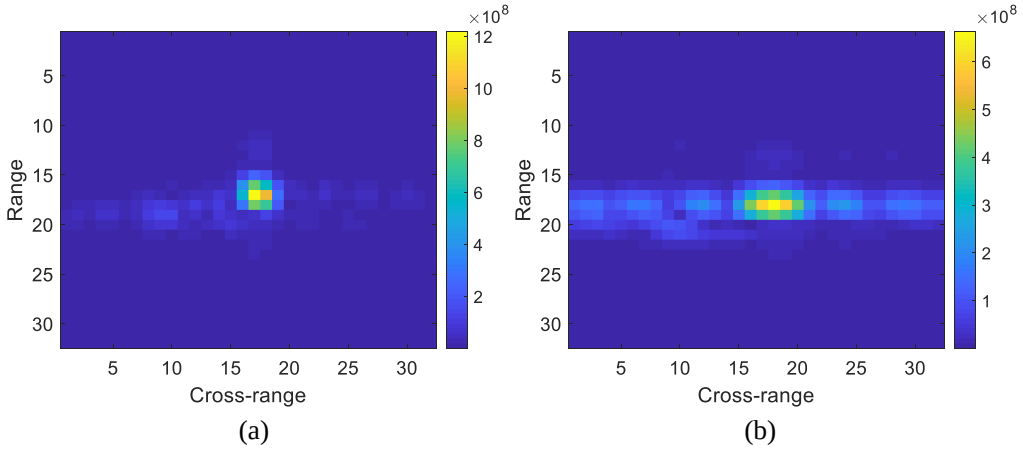

Figure 17. The imaging result of T3. (**a**) HPC-GMTIm (entropy = 2.48). (**b**) GHHAF method (entropy = 2.81).

4.4. T4

Figure 18 shows the SAR image containing target T4. It can be seen that the energy of T4 spread along a horizontal road. Similar to the detection of T2, multiple subaperture images were used to extract the energy of T4, as shown in Figure 19. Transferring the detected signal in Figure 19b back to the range-compressed and cross-range slow time domain, we obtained the target envelope in Figure 20a. Since there is no obvious range cell migration in Figure 20a, it can be deduced that the defocusing was mainly caused by the cross-range motion parameters. After the RCMC using the proposed HPC-GMTIm algorithm, the envelope of T4 is plotted in Figure 20b, which is straighter than the one in Figure 20a. The final imaging result is given in Figure 21, where the HPC-GMTIm still outperformed the GHHAF method.

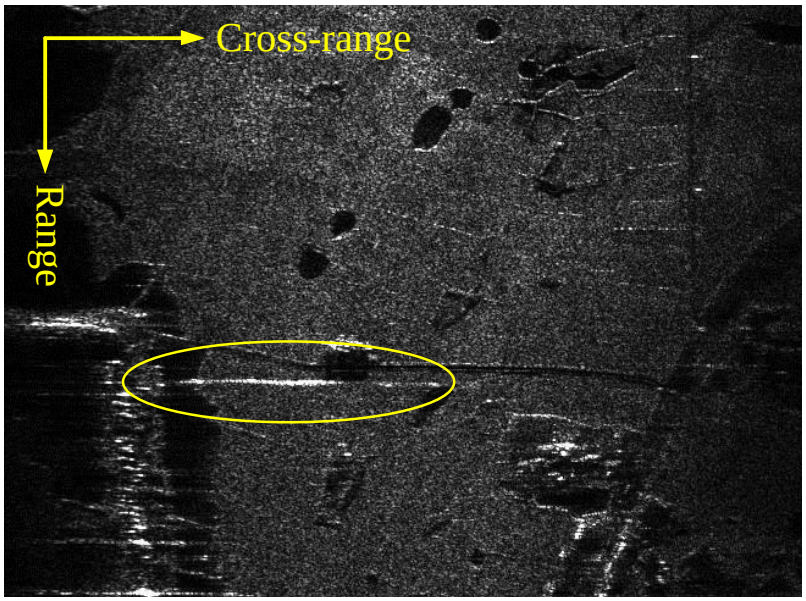

Figure 18. The stationary scene containing moving target T4.

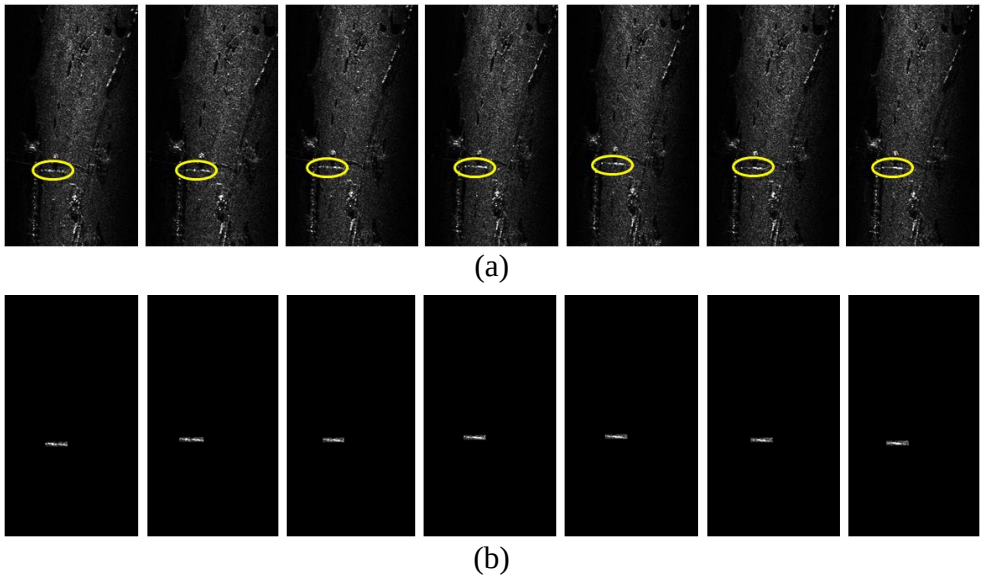

Figure 19. Moving target detection for T4. (**a**) Subaperture images before detection. (**b**) Subaperture images after detection.

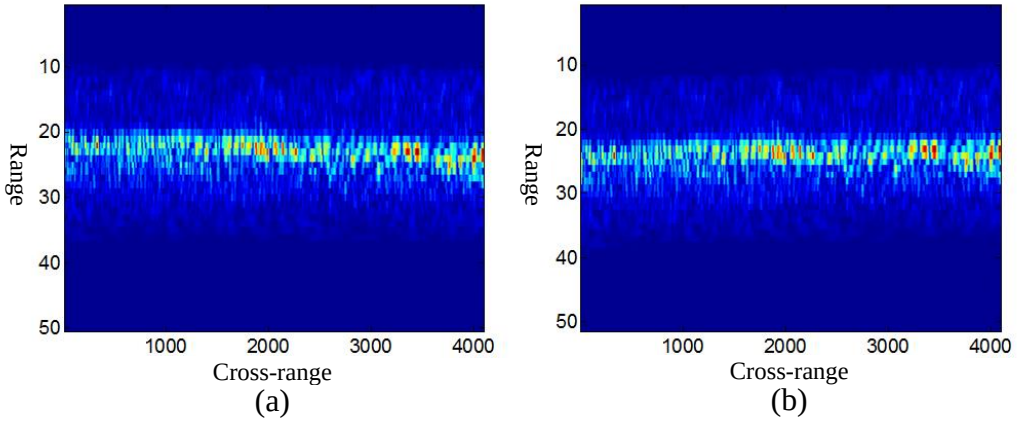

Figure 20. The envelope of T4. (**a**) Before RCMC. (**b**) After RCMC.

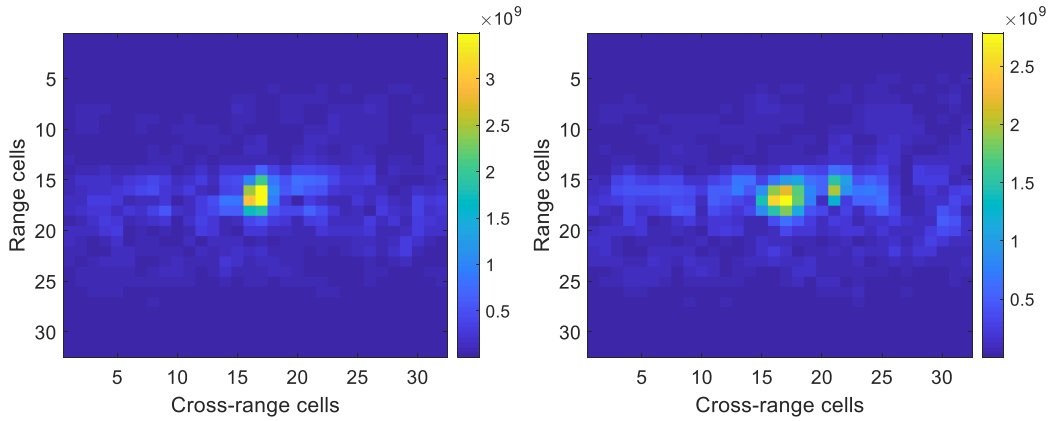

Figure 21. The imaging result of T4. (**a**) HPC-GMTIm (entropy = 3.46). (**b**) GHHAF method (entropy = 4.03).

5. Conclusions

An improved GMTIm algorithm, named the HPC-GMTIm, was proposed in this paper, which is suitable for high-squint SAR mode and capable of estimating more high-order phase terms in comparison with the existing methods. In the HPC-GMTIm algorithm, it is assumed that the moving target has a constant velocity in the subaperture CPI and maneuvering motion in the whole CPI. As a result, the echoed signal can be approximated by a three-order polynomial in the subaperture CPI and a high-order one for the whole CPI. From the estimation results of the subaperture processing, the instantaneous DF was obtained. By combining the instantaneous DF elements from the subapertures into a linear system of equations, the high-order polynomial coefficients for the whole CPI can be determined by a TLS solver. The proposed GMTIm algorithm is flexible for various polynomial signals.

Author Contributions: L.R. conceived of the main idea, designed the experiments, and wrote the manuscript. Z.L. and R.X. provided the experimental data and reviewed the manuscript. All authors have read and agreed to the published version of the manuscript.

Funding: This work was funded in part by the National Natural Science Foundation of China under Grant 62001346 and the China Postdoctoral Science Foundation under Grant 2019M663632 and Grant XJS210202. It was also funded by the Science and Technology on Plasma Dynamics Laboratory, Air Force Engineering University, No. 6142202210305, and the Seed Funding Project of Multisensor Intelligent Detection and Recognition Technologies R&D Center of CASC, No. ZZJJ202102.

Institutional Review Board Statement: Not applicable.

Informed Consent Statement: Not applicable.

Data Availability Statement: Not applicable.

Acknowledgments: The authors would like to thank the anonymous Reviewers for their valuable comments, which improved the paper's quality.

Conflicts of Interest: The authors declare no conflict of interest.

References

1. Cumming, G.; Wong, F.H. *Digital Processing of Synthetic Aperture Radar Data: Algorithms and Implementation*; Artech House: Norwood, MA, USA, 2005.
2. Ran, L.; Xie, R.; Liu, Z.; Zhang, L.; Li, T.; Wang, J. Simultaneous Range and Cross-Range Variant Phase Error Estimation and Compensation for Highly Squinted SAR Imaging. *IEEE Trans. Geosci. Remote Sens.* **2018**, *56*, 4448–4463. [CrossRef]
3. Ran, L.; Liu, Z.; Xie, R.; Zhang, L. Focusing High-Squint Synthetic Aperture Radar Data Based on Factorized Back-Projection and Precise Spectrum Fusion. *Remote Sens.* **2019**, *11*, 2885. [CrossRef]
4. Li, Z.; Huang, C.; Sun, Z.; An, H.; Wu, J.; Yang, J. BeiDou-Based Passive Multistatic Radar Maritime Moving Target Detection Technique via Space–Time Hybrid Integration Processing. *IEEE Trans. Geosci. Remote Sens.* **2021**, *60*, 5802313. [CrossRef]

5. Devoreand, M.D.; Sullivan, J.A.O. Performance complexity study of several approaches to automatic target recognition from SAR images. *IEEE Trans. Aerosp. Electron. Syst.* **2002**, *38*, 632–648.
6. Noviello, C.; Fornaro, G.; Martorella, M. Focused SAR Image Formation of Moving Targets Based on Doppler Parameter Estimation. *IEEE Trans. Geosci. Remote Sens.* **2015**, *53*, 3460–3470. [CrossRef]
7. Kirscht, M.; Mietzner, J.; Bickert, B.; Dallinger, A.; Hippler, J.; Meyer-Hilberg, J.; Zahn, R.; Boukamp, J. An Airborne Radar Sensor for Maritime and Ground Surveillance and Reconnaissance–Algorithmic Issues and Exemplary Results. *IEEE J. Sel. Top. Appl. Earth Obs. Remote Sens.* **2015**, *9*, 971–979. [CrossRef]
8. Pelich, R.-M.; Longepe, N.; Mercier, G.; Hajduch, G.; Garello, R. Vessel Refocusing and Velocity Estimation on SAR Imagery Using the Fractional Fourier Transform. *IEEE Trans. Geosci. Remote Sens.* **2016**, *54*, 1670–1684. [CrossRef]
9. Li, Z.; Zhang, X.; Yang, Q.; Xiao, Y.; An, H.; Yang, H.; Wu, J.; Yang, J. Hybrid SAR-ISAR Image Formation via Joint FrFT-WVD Processing for BFSAR Ship Target High-Resolution Imaging. *IEEE Trans. Geosci. Remote Sens.* **2021**, *60*, 5215713. [CrossRef]
10. Gorovyi, M.; Sharapov, D.S. A novel algorithm for estimation of moving target parameters with single-antenna SAR. In Proceedings of the 2016 International Conference on Mathematical Methods in Electromagnetic Theory, Lviv, Ukraine, 5–7 July 2016; pp. 188–191.
11. Yang, J.; Liu, C.; Wang, Y. Imaging and parameter estimation of fast-moving targets with single-antenna SAR. *IEEE Geosci. Remote Sens. Lett.* **2014**, *11*, 529–533. [CrossRef]
12. Zheng, H.; Liu, Q.; Liu, H. Parameterized centroid frequency-chirp rate distribution for LFM signal analysis and mechanisms of constant delay introduction. *IEEE Trans. Signal Process.* **2017**, *65*, 6435–6447. [CrossRef]
13. Huang, P.; Liao, G.; Yang, Z.; Xia, X.-G.; Ma, J.-T.; Ma, J. Long-Time Coherent Integration for Weak Maneuvering Target Detection and High-Order Motion Parameter Estimation Based on Keystone Transform. *IEEE Trans. Signal Process.* **2016**, *64*, 4013–4026. [CrossRef]
14. Yang, J.; Liu, C.; Wang, Y. Detection and Imaging of Ground Moving Targets With Real SAR Data. *IEEE Trans. Geosci. Remote Sens.* **2015**, *53*, 920–932. [CrossRef]
15. Zhu, D.; Li, Y.; Zhu, Z. A Keystone Transform Without Interpolation for SAR Ground Moving-Target Imaging. *IEEE Geosci. Remote Sens. Lett.* **2007**, *4*, 18–22. [CrossRef]
16. Li, G.; Xia, X.-G.; Peng, Y.-N. Doppler Keystone Transform: An Approach Suitable for Parallel Implementation of SAR Moving Target Imaging. *IEEE Geosci. Remote Sens. Lett.* **2008**, *5*, 573–577. [CrossRef]
17. Sun, G.; Xing, M.; Xia, X.-G.; Wu, Y.; Bao, Z. Robust Ground Moving-Target Imaging Using Deramp–Keystone Processing. *IEEE Trans. Geosci. Remote Sens.* **2013**, *51*, 966–982. [CrossRef]
18. Huang, P.; Liao, G.; Yang, Z.; Xia, X.-G.; Ma, J.; Zheng, J. Ground Maneuvering Target Imaging and High-Order Motion Parameter Estimation Based on Second-Order Keystone and Generalized Hough-HAF Transform. *IEEE Trans. Geosci. Remote Sens.* **2016**, *55*, 320–335. [CrossRef]
19. Yang, J.; Zhang, Y. An Airborne SAR Moving Target Imaging and Motion Parameters Estimation Algorithm With Azimuth-Dechirping and the Second-Order Keystone Transform Applied. *IEEE J. Sel. Top. Appl. Earth Obs. Remote Sens.* **2015**, *8*, 3967–3976. [CrossRef]
20. Almeida, B. The fractional fourier transform and time–frequency representations. *IEEE Trans. Signal Process.* **1994**, *42*, 3084–3091. [CrossRef]
21. Ozaktas, H.M.; Ankan, O.; Alper Kutay, M.; Bozdavgi, G. Digital computation of the fractional fourier transform. *IEEE Trans. Signal. Process.* **1996**, *44*, 2141–2150. [CrossRef]
22. Tao, R.; Li, Y.-L.; Wang, Y. Short-Time Fractional Fourier Transform and Its Applications. *IEEE Trans. Signal. Process.* **2010**, *58*, 2568–2580. [CrossRef]
23. Liang, Y.; Li, Z.; Zeng, L.; Xing, M.; Bao, Z. A High-Order Phase Correction Approach for Focusing HS-SAR Small-Aperture Data of High-Speed Moving Platforms. *IEEE J. Sel. Top. Appl. Earth Obs. Remote Sens.* **2015**, *8*, 4551–4561. [CrossRef]
24. Zheng, J.; Chen, R.; Yang, T.; Liu, X.; Liu, H.; Su, T.; Wan, L. An Efficient Strategy for Accurate Detection and Localization of UAV Swarms. *IEEE Internet Things J.* **2021**, *8*, 15372–15381. [CrossRef]
25. Hirakawa, K.; Parks, T.W. Image denoising using total least squares. *IEEE Trans. Image Process.* **2006**, *15*, 2730–2742. [CrossRef] [PubMed]
26. Schaffrin, B.; Wieser, A. On weighted total least-squares adjustment for linear regression. *J. Geodesy* **2008**, *82*, 415–421. [CrossRef]
27. Zheng, J.; Yang, T.; Liu, H.; Su, T.; Wan, L. Accurate Detection and Localization of Unmanned Aerial Vehicle Swarms-Enabled Mobile Edge Computing System. *IEEE Trans. Ind. Inform.* **2021**, *17*, 5059–5067. [CrossRef]
28. Kim, M.; Memon, S.A.; Shin, M.; Son, H. Dynamic based trajectory estimation and tracking in an uncertain environment. *Expert Syst. Appl.* **2021**, *177*, 114919. [CrossRef]
29. Memon, S.A.; Ullah, I. Detection and tracking of the trajectories of dynamic UAVs in restricted and cluttered environment. *Expert Syst. Appl.* **2021**, *183*, 115309. [CrossRef]
30. Asad, M.; Khan, S.; Ihsanullah; Mehmood, Z.; Shi, Y.; Memon, S.A.; Khan, U. A split target detection and tracking algorithm for ballistic missile tracking during the re-entry phase. *Def. Technol.* **2019**, *16*, 1142–1150. [CrossRef]
31. Ran, L.; Liu, Z.; Zhang, L.; Li, T.; Xie, R. An Autofocus Algorithm for Estimating Residual Trajectory Deviations in Synthetic Aperture Radar. *IEEE Trans. Geosci. Remote Sens.* **2017**, *55*, 3408–3425. [CrossRef]
32. Ran, L.; Liu, Z.; Li, T.; Xie, R.; Zhang, L. Extension of Map-Drift Algorithm for Highly Squinted SAR Autofocus. *IEEE J. Sel. Top. Appl. Earth Obs. Remote Sens.* **2017**, *10*, 4032–4044. [CrossRef]

33. Bai, X.; Tao, R.; Wang, Z.; Wang, Y. ISAR Imaging of a Ship Target Based on Parameter Estimation of Multicomponent Quadratic Frequency-Modulated Signals. *IEEE Trans. Geosci. Remote Sens.* **2013**, *52*, 1418–1429. [CrossRef]
34. Noviello, C.; Fornaro, G.; Braca, P.; Martorella, M. Fast and Accurate ISAR Focusing Based on a Doppler Parameter Estimation Algorithm. *IEEE Geosci. Remote Sens. Lett.* **2017**, *14*, 349–353. [CrossRef]